Structural, Magnetic, and Electronic Properties of a Pentacoordinated Intermediate-Spin ($S = {}^3/_2$) Iron(III) Complex with a Macrocyclic [N$_4$]$^{2-}$ Ligand

H. Keutel,[†] I. Käpplinger,[†] E.-G. Jäger,*,[†] M. Grodzicki,*,[‡] V. Schünemann,[§] and A. X. Trautwein*,[§]

Institut für Anorganische und Analytische Chemie, Friedrich-Schiller-Universität Jena, August-Bebel-Strasse 2, D-07743 Jena, Germany, Institut für Mineralogie, Universität Salzburg, Hellbrunner Strasse 34, A-5020 Salzburg, Austria, and Institut für Physik, Medizinische Universität Lübeck, Ratzeburger Allee 160, D-23538 Lübeck, Germany

The complex (6,13-bis(ethoxycarbonyl)-5,14-dimethyl-1,4,8,11-tetraazacyclotetradeca-4,6,12,14-tetraenato(2−))-iron(III) iodide, **3** (chemical formula C$_{18}$H$_{26}$O$_4$N$_4$FeI·0.5 C$_7$H$_8$), has been characterized by X-ray crystallography ($a = 16.063(3)$ Å, $b = 15.895(3)$ Å, $c = 19.703(4)$ Å, $\beta = 107.11(3)°$; monoclinic; $I2/a$; $Z = 8$), EPR and Mössbauer spectroscopy, and temperature-dependent magnetic susceptibility as well as by MO calculations. The pentacoordinated iron atom is 0.34 Å outside of the [N$_4$] plane. The equatorial Fe−N distances (1.92 Å for the N's in neighborhood of the methylated C-atoms and 1.88 Å for the others) are not significantly different from those found in octahedral low-spin iron(III) complexes with the same macrocyclic [N$_4$$^{2-}$] ligand. The magnetic moment ($\mu_{eff} = 4.19$ μ_B up to 20 K; $\Theta = -7.37$ K), the EPR measurements ($g_y{}^{eff} = 5.38$, $g_x{}^{eff} = 2.70$, and $g_z{}^{eff} = 1.74$), and the Mössbauer data ($\delta = 0.18$ mm/s, $\Delta E_Q = 3.56$ mm/s, $T = 120$ K) indicate a pure intermediate-spin state of $S = {}^3/_2$. The MO calculations yield a complete picture of bonding modes, intramolecular interactions, and the electronic structure around the iron center, as indicated by the correct determination of the ground state and by the agreement between the measured and calculated quadrupole splitting.

Introduction

Iron porphyrins play an outstanding role as active sites of many enzymes. Especially the spin states and their changes with the accompanying geometrical changes of the porphyrins are of central importance regarding the catalytic as well as the charge-transfer properties of these enzymes. Besides the typical octahedral low-spin and pentacoordinated high-spin iron(III) porphyrins,[1] a quantum-mechanically admixed intermediate spin was found in the case of ferricytochrome *c′*.[2,3]

Investigations on different model Fe(III) porphyrins and phthalocyanines show that it is difficult to stabilize the intermediate spin with these equatorial [N$_4$]$^{2-}$ macrocycles. Low-spin species were found in the case of all octahedrally coordinated complexes with two moderate- to strong-field axial ligands (e.g. imidazole, pyridine).[4] The pentacoordinated porphyrins with ligands as halides or sulfides show high-spin behavior ($S = 5/2$).[5] In the case of weakly coordinated complexes with ClO$_4$$^-$ or SbF$_6$$^-$ anions,[6] in strongly distorted complexes with halides,[7] and in octahedral complexes with very weak bases (3-chloropyridine,[8] tricyanomethanide,[9] H$_2$O/OSO$_2$-CF$_3$[10]) as well as in pentacoordinated phthalocyanines[11] not a pure intermediate but a quantum-mechanically admixed spin state ($S = {}^3/_2, {}^5/_2$) was found.

Pure intermediate spin states of iron(III) have been detected only in few cases, viz. in some pentacoordinated halide complexes with thiocarbamates,[12] thiosalen,[13] or the carbonyl free [N$_4$]$^{2-}$ macrocycles **1** (Chart 1) (X, Y = ethylene, trimethylene; R^1 = R^3 = H, R^2 = Ph;[14] R^1 = R^2 = H, R^3 =

[†] Friedrich-Schiller-Universität Jena.

[‡] Universität Salzburg.

[§] Medizinische Universität Lübeck.

(1) Scheidt, W. R.; Reed, C. A. *Chem. Rev.* **1981,** *81,* 543−555.

(2) Mitra, S. In *Iron Porphyrins*, 1st ed.; Lever, A. B. P., Gray, H. B., Eds.; Addison-Wesley Publishing Co., Inc.: Reading, MA, 1983; Vol. 2, pp 1−42.

(3) Maltempo, M. M. *J. Chem. Phys.* **1974,** *61,* 2540−2547.

(4) Walker, F. A.; Reis, D.; Balke, V. L. *J. Am. Chem. Soc.* **1984,** *106,* 6, 6888−6898.

(5) (a) Anzai, K.; Hatano, K.; Lee, Y. J.; Scheidt, W. R. *Inorg. Chem.* **1981,** *20,* 2337−2339. (b) Hoard, J. L.; Cohen, G. H.; Glick, M. D. *J. Am. Chem. Soc.* **1967,** *89,* 1992−1996. (c) Hatano, K.; Scheidt, W. R. *Inorg. Chem.* **1979,** *18,* 877−879. (d) Zhang, Y.; Hallows, W. A.; Ryan, W. J.; Jones, J. G.; Carpenter, G. B.; Sweigart, D. A. *Inorg. Chem.* **1994,** *33,* 3306−3312.

(6) (a) Reed, C. A.; Mashiko, T.; Bentley, St. P.; Kastner, M. E.; Scheidt, W. R.; Spartalian, K.; Lang, G. *J. Am. Chem. Soc.* **1979,** *23,* 2948−2958. (b) Shelly, K.; Barthczak, T.; Scheidt, W. R.; Reed, C. A. *Inorg. Chem.* **1985,** *24,* 4325−4330.

(7) Cheng, R.-J.; Chen, P.-Y.; Gau, P.-R.; Chen, C.-C.; Peng, S.-M. *J. Am. Chem. Soc.* **1997,** *119,* 2563−2569.

(8) Scheidt, W. R.; Geiger, D. K.; Hayes, R. G.; Lang, G. *J. Am. Chem. Soc.* **1983,** *105,* 2625−2632.

(9) Summerville, D. A.; Cohen, I. A.; Hatano, K.; Scheidt, W. R. *Inorg. Chem.* **1978,** *17,* 2906−2910.

(10) Gismelseed, A.; Bominaar, E. L.; Bill, E.; Trautwein, A. X.; Winkler, H.; Nasri, H.; Doppelt, P.; Mandon, D.; Fischer, J.; Weiss, R. *Inorg. Chem.* **1990,** *29,* 2741.
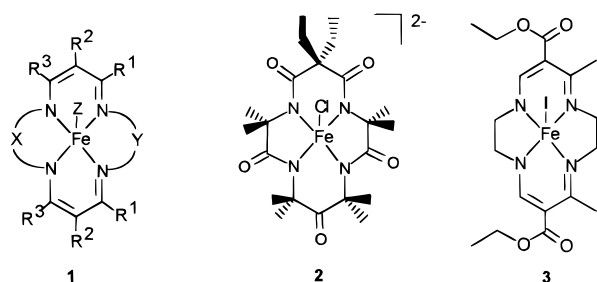
(11) Kennedy, B. J.; Murray, K. S.; Homborg, H.; Kalz, W. *Inorg. Chem.* **1986,** *25,* 2539−2545.

(12) (a) Martin, R. L.; White, A. H. *Inorg. Chem.* **1967,** *6,* 712−717. (b) Healy, P. C.; White, A. H. *J. Chem. Soc., Dalton Trans.* **1972,** *1,* 1369−1372. (c) Kepert, D. L.; Raston, C. L.; White, A. H. *J. Chem. Soc., Dalton Trans.* **1980,** *9,* 1921−1927. (d) DeFotis, G. D.; Harlan, E. W.; Jarvis, W. R. A.; Terranova, V. J.; Pugh, V. J.; Marmorino, J. L.; Hogg, B. D.; Jensen, T. R. *J. Magn. Mater.* **1996,** *154,* 83−95.

(13) (a) Fallon, G. D.; Gatehouse, B. M.; Marini, P. J.; Murray, K. S.; West, B. O. *J. Chem. Soc., Dalton Trans.* **1984,** *4,* 2733−2739.

(14) Koch, S.; Holm, R. H.; Frankel, R. B. *J. Am. Chem. Soc.* **1975,** *97,* 6714−6723.

Chart 1

1a: R^1 = Me, R^2 = COOEt, R^3 = H,
   X = 1,2-C_6H_4, Y = C_2H_4, Z = I;

1b: R^1 = Me, R^2 = COOEt, R^3 = H,
   X = Y = 1,2-C_6H_4, Z = I;

1c: $R^1 = R^3$ = Me, R^2 = H,
   X = Y = 1,2-C_6H_4, Z = Cl.

Me[15]) as well as the oxo-functionalized $[N_4]^{4-}$ macrocycle in **2**[16] as equatorial chelate ligands. These examples show that such a spin state is stabilized in case of the strongly tetragonally distorted pentacoordinated halides, acetates, and sulfides of iron-(III) $[N_4]$ macrocycles **1** and **2** exerting a strong ligand field.[14-16]

These differences in the spin state have been explained with ligand field effects on the d-orbital splitting.[6a,10] Holm et al.[14] showed that in the case of the pentacoordinated complexes **1** ($R^1 = R^3$ = H, R^2 = Ph) the spin multiplicity was reduced, if the axial field component increased or the ring size decreased, and therefore the corresponding equatorial field component increased.

As part of a program to investigate the electronic structure of 3d-metal complexes with varying macrocyclic ligands which are not porphin derivatives but have a similar equatorial $[N_4]^{2-}$ donor set, we synthesized the iron(III) complex **3** and its ethylene/phenylene and phenylene/phenylene bridged analogs, which belong to the general class of the complexes **1**.[17] Recently, we reported about the spectroscopic properties of the octahedral diadducts,[18] the equilibria and kinetics of the stepwise substitution of axial ligands,[19] the redox potentials,[19] and the catalytic performance of these complexes.[20] Preliminary measurements of the magnetic susceptibility of **3** showed a temperature-independent magnetic moment of approximately 4 μ_B at 77 K,[18] indicating a pure intermediate spin state ($S = {}^3/_2$).

Now we crystallized complex **3** and solved its structure. By this means it became possible to evaluate the electronic structure by molecular orbital calculations in local density approximation. Including the results of magnetic measurements as well as EPR and Mössbauer spectroscopy, we are able to give a comprehensive characterization of the electronic structure and to describe in detail the reasons for the existence of the pure intermediate spin state.

Materials and Methods

Synthesis. The iron(III) complex **3** was prepared as described previously.[21] Crystals were obtained by extraction of 3 g of **3** with 40 mL of toluene and slow cooling of the hot solution. X-ray-quality

Table 1. Experimental Data for the Structure Determination of **3**

chem formula	$C_{18}H_{26}O_4N_4FeI \cdot 0.5C_7H_8$
M_r, g/mol	591.24
space group	$I2/a$ (No. 15)
a, Å	16.063(3)
b, Å	15.895(3)
c, Å	19.703(4)
β, deg	107.11(3)
V, Å^3	4808(2)
Z	8
ρ_{calcd}, g/cm^3	1.634
$\mu_{MoK\alpha}$, cm^{-1}	19.46
T, K	183
$F_o > 4\sigma(F_o)$	4723
$I > 4\sigma(I)$	6894
R^a	0.0389
$wR2^b$	0.0833
λ, Å	0.710 73

^{a} $R = (\sum||F_o| - |F_c||)/\sum|F_o|$. ^{b} $wR2 = \{\sum[w(F_o^2 - F_c^2)^2]/\sum[w(F_o^2)^2]\}^{1/2}$.

crystals were obtained within 24 h. Anal. Calcd for $C_{18}H_{26}N_4FeIO_4 \cdot {}^1/_2C_7H_8$: C, 43.67; H, 5.11; N, 9.48; Fe, 9.45; I, 21.46. Found: C, 43.77; H, 5.10; N, 9.51; Fe, 9.57; I, 21.06.

X-ray Crystal Structure Determination. A crystal of **3** was mounted with paraffin oil on a glass fiber on an Enraf-Nonius CAD 4 diffractometer. Data were collected using Mo Kα radiation (λ = 0.7107 Å). The unit cell parameters were obtained by a least-squares fit of 25 reflections. The solution and refinement were done by using SHELXS-86[22] and SHELXL-93,[23] respectively. The structure was solved by the Patterson method and refined by full-matrix least-squares against F^2. All non-hydrogen atoms were refined anisotropically. The positions of the hydrogen atoms were calculated at a distance of 0.96 Å. Further data can be requested from Fachinformationszentrum *Karlsruhe* (FIZ), D-763344 Eggenstein-Leopoldshafen, (e-mail: crysdata@fiz-karlsruhe.de), by quoting CSD No. 408790. The cell constants and other pertinent data were collected and are recorded in Table 1.

Magnetic Susceptibility. The solid-state magnetic susceptibilities were measured from 300 K down to 1.73 K at magnetic fields of 0.5 and 0.8 T by the SQUID method on a Quantum Design MPMS 2. Diamagnetic corrections for the ligands were accounted for by methods described in the literature.[24]

Mössbauer Spectroscopy. Mössbauer spectra were recorded using a conventional spectrometer in the constant acceleration mode. Isomer shifts are given relative to α-Fe at room temperature. The spectra obtained at low fields (20 mT) were measured in a He-bath cryostat (Oxford Instruments, MD 306) equipped with a pair of circular permanent magnets. For the high-field spectra a cryostat with a superconducting magnet was used (Oxford Spectromag 4000M). Magnetically split spectra of paramagnetic samples were simulated on the basis of the spin-Hamiltonian approximation described below; otherwise spectra were analyzed by least-squares fits using Lorentzian line shape.

EPR Spectroscopy. EPR spectra were recorded with a conventional X-band spectrometer (Bruker 200D SRC) equipped with a He-flow cryostat (ESR 910, Oxford Instruments) in a temperature range of T = 6-40 K.

Spin Hamiltonian Formalism. The analyses of magnetic Mössbauer and EPR spectra were carried out on the basis of the spin Hamiltonian for $S = {}^3/_2$:

(15) Riley, D. P.; Busch, D. H. *Inorg. Chem.* **1984**, *23*, 3235-3241.
(16) Kostka, K. L.; Fox, B. G.; Hendrich, M. P.; Collins, T. J.; Rickard, C. E. F.; Wright, L. J.; Münck, E. *J. Am. Chem. Soc.* **1993**, *115*, 6746-6757.
(17) Jäger, E.-G.; Keutel, H.; Rudolph, M.; Krebs, B.; Wiesemann, F. *Chem. Ber.* **1995**, *128*, 503-514.
(18) Jäger, E.-G.; Keutel, H. *Inorg. Chem.* **1997**, *36*, 3512-3519.
(19) Jäger, E.-G.; Keutel, H.; Barth, S. In *Deutsche Forschungsgemeinschaft: Bioinorganic Chemistry—Transition Metals in Biology and their Coordination Chemistry*; Trautwein, A. X., Ed.; Wiley-VCH: New York, 1997; pp 584-605.
(20) (a) Jäger, E.-G.; Knaudt, J.; Rudolph, M.; Rost, M. *Chem. Ber.* **1996**, *129*, 1041-1047. (b) Knaudt, J. Ph.D. Thesis, University of Jena, 1998.
(21) Jäger, E.-G.; Hähnel, H.; Klein, H.-F.; Schmidt, A. *J. Prakt. Chem.* **1991**, *333*, 423-430.
(22) Sheldrick, G. M. *SHELXS-86, A Computer Program for Crystal Structure Solution*; University of Göttingen: Göttingen, Germany, 1986.
(23) Sheldrick, G. M. *SHELXS-93, A Computer Program for Crystal Structure Refinement*; University of Göttingen: Göttingen, Germany, 1993.
(24) Kahn, O. *Molecular Magnetism;* VCH Publishers: New York, Weinheim, Cambridge, 1993; p 3.

$$\hat{H}_{\text{eff}} = D\left[\hat{S}_z^2 - \frac{1}{3}S(S+1) + \frac{E}{D}(\hat{S}_x^2 - \hat{S}_y^2)\right] + \mu_B \vec{S}\tilde{g}\vec{B} \qquad (1)$$

D denotes the zero-field splitting parameter, and E/D, the rhombicity parameter. $\vec{B}$ is the external field, $\tilde{g}$ the electronic g tensor, and μ_B the Bohr magneton. High-field Mössbauer spectra were simulated using eq 1 together with the nuclear Hamiltonian

$$\hat{H}_N = \frac{eQV_{zz}}{4I(2I-1)}[3\hat{I}_z^2 - I(I+1) + \eta(\hat{I}_x^2 - \hat{I}_y^2)] - g_N\mu_N\vec{I}\vec{B} + \langle\vec{S}\rangle\tilde{A}\vec{I} \qquad (2)$$

Here I denotes the nuclear spin quantum number, Q the nuclear quadrupole moment of the excited nuclear state, V_{zz} the main component of the electric-field gradient (efg) tensor, and $\eta = (V_{yy} - V_{xx})/V_{zz}$ is the asymmetry parameter of the efg. $\tilde{A}$ denotes the hyperfine coupling tensor, and g_N, the nuclear g factor.
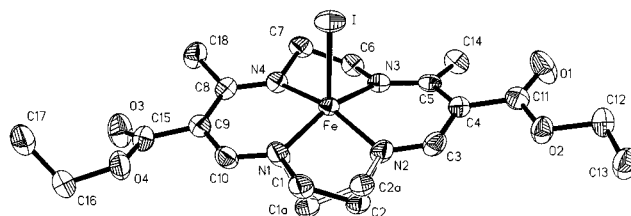
Theoretical Methods. Molecular orbital (MO) calculations have been carried out in local density approximation (LDA)[25,26] by the spin-polarized self-consistent-charge (SCC-) Xα method.[27–29] The Mössbauer parameters, viz. the isomer shift and the quadrupole splitting, have been calculated as described in detail previously.[30] The measured quadrupole splitting ΔE_Q is related to the components $|V_{zz}| \geq |V_{yy}| \geq |V_{xx}|$ of the electric field gradient (efg) tensor in its principal axes system by

$$\Delta E_Q = \frac{1}{2}eQV_{zz}\left(1 + \frac{\eta^2}{3}\right)^{1/2} \qquad (3)$$

with the nuclear quadrupole moment $Q = 0.15$ barn.[31] Core polarization effects are taken into account by the Sternheimer shielding function $\gamma(r)$ derived from atomic self-consistent first-order perturbation calculations.[32] Apart from these approximations, the efg tensor is computed rigorously within the frame of a valence-electron-only MO method.[30]

Results and Discussion

X-ray Structural Studies. The complex **3** crystallizes in the monoclinic system with the space group $I2/a$ including 8 molecules of **3** and 4 molecules of toluene in the unit cell. An ORTEP drawing of the complex is displayed in Figure 1. Selected atomic distances and angles are listed in Table 2. The iron atom has an approximately square pyramidal coordination and is located 0.34 Å above the plane of the four nitrogen atoms. The Fe–N distances are about 1.92 Å for the nitrogen atoms in neighborhood of the methylated C-atoms and 1.88 Å for the others. The N–Fe–N angles reflect the low symmetry of the macrocycle with its alternating five- and six-membered chelate rings. The Fe–I bond (2.673(1) Å) is perpendicular to the N$_4$ plane (89.7(2)°). The main planes including the ligand atoms of the six-membered chelate rings (B and C in Table 2) are tilted away from the N$_4$ plane by 7.1 or 7.2°, respectively. Their π-system is delocalized as indicated by the bond distances (cf. Table 2). The carbonyl groups are twisted with respect to the six-membered rings by 8.6 and 20.1°, respectively. The methyl

(25) Parr, R. G.; Yang, W. *Density Functional Theory of Atoms and Molecules*; Oxford University Press: New York, 1989.
(26) *Local Density Approximations in Quantum Chemistry and Solid State Physics*; Dahl, J. P., Avery, J., Eds.; Plenum Press: New York, London, 1984.
(27) Grodzicki, M. *J. Phys. B* **1980**, *13*, 2683.
(28) Grodzicki, M. Theory and Applications of the Self-Consistent-Charge Xα Method. Thesis of habilitation, Hamburg, Germany, 1985.
(29) Bläs, R.; Guillin, J.; Bominaar, E. L.; Grodzicki, M.; Marathe, V. R.; Trautwein, A. X. *J. Phys. B* **1987**, *20*, 5627.
(30) Grodzicki, M.; Männing, V.; Trautwein, A. X.; Friedt, J. M. *J. Phys. B* **1987**, *20*, 5595.
(31) Bominaar, E. L.; Guillin, J.; Sawaryn, A.; Trautwein, A. X. *Phys. Rev. B* **1989**, *39*, 72.
(32) Lauer, S.; Marathe, V. R.; Trautwein, A. X. *Phys. Rev. A* **1979**, *19*, 1852.

Figure 1. ORTEP plot and numbering scheme used for **3**. Thermal ellipsoids are at the 50% level.

Table 2. Selected Bond Lengths (Å) and Angles (deg) for **3**

N(1)–Fe	1.892(3)	Fe–I	2.637(1)
N(2)–Fe	1.884(3)	N(3)–C(5)	1.319(5)
N(3)–Fe	1.925(3)	C(5)–C(4)	1.440(5)
N(4)–Fe	1.924(3)	C(4)–C(3)	1.412(5)
N(4)–C(7)	1.468(5)	C(3)–N(2)	1.307(5)
C(7)–C(6)	1.503(6)	C(4)–C(11)	1.460(6)
N(3)–C(6)	1.480(5)		
N(2)–Fe–N(1)	83.9(2)	N(2)–Fe–I	99.60(12)
N(1)–Fe–N(4)	91.53(14)	N(1)–Fe–I	100.97(12)
N(2)–Fe–N(3)	90.19(14)	N(4)–Fe–I	99.97(9)
N(4)–Fe–N(3)	86.94(13)	N(3)–Fe–I	100.96(9)
N(2)–C(3)–C(4)	125.8(4)	C(3)–C(4)–C(5)	121.4(3)
C(4)–C(5)–N(3)	120.4(3)		
N(3)–C(6)–C(7)–N(4)^a	−42.1	B–A^b	7.2
N(1)–C(1)–C(2)–N(2)	46.9	C–A	7.1
N(1)–C(1a)–C(2a)–N(2)	−51.9		
C(5)–C(4)–C(11)–O(1)	9.3		
C(8)–C(9)–C(15)–O(3)	20.7		

^{a} Torsion angles (deg). ^{b} Angles between the main planes with the following atoms: A, N(1), N(2), N(3), N(4); B, N(2), C(3), C(4), C(5), N(3); C, N(1), C(10), C(9), C(8), N(4).

groups at the chelate rings (R^3) are arranged in *cis* configuration to each other.

The ethylene bridges of the five-membered chelate rings exhibit a *twist* conformation with torsion angles of −42.1 and 46.9 or −51.9°, respectively. The C-atoms of the ethylene bridge in the part of the molecule without methyl groups are disordered.

Figure 2 shows the packing of the molecules in the crystal. The molecules are arranged in double layers, which are separated from each other by toluene with a distance of 4.13 Å. Within the double layer the distance between the molecular layers is 2.92 Å. The Fe–I bonds of one layer are directed toward the other layer in such a way that they point into the void space between two molecules of the second layer (the minimum distance of iodine to an atom within this layer is 3.98 Å).

The spin state of the iron is mainly determined by its first coordination sphere. In Table 3, some characteristic bond distances of related iron(III) complexes are collected. In comparison of the Fe–N$_{eq}$ and Fe–ct distances, the following remarkable facts can be noted: (i) Both intermediate spin complexes **2** and **3** have approximately the same Fe–N$_{eq}$ and Fe-ct distances. (ii) In the change from the pentacoordinated intermediate-spin complex **3** to its octahedral low-spin derivative with two axial imidazoles (**3**(HIm)$_2$PF$_6$ in Table 3)[33] the Fe–N$_{eq}$ distances do not change with increasing coordination number (5 to 6) and decreasing spin multiplicity ($S = 3/2$ to $S = 1/2$). (iii) In the structurally similar high-spin complex **1c** the Fe–N$_{eq}$ distances are increased by about 0.1 Å.[34] (iv) In the case of pentacoordinated iron(III) porphyrins with admixed spin states,

(33) Wiesemann, F.; Wonnemann, R.; Krebs, B.; Keutel, H.; Jäger, E.-G. *Angew. Chem., Int. Ed. Engl.* **1994**, *33*, 1363–1366.
(34) Weiss, M. C.; Bursten, B.; Peng, S.-M.; Goedken, V. L. *J. Am. Chem. Soc.* **1976**, *98*, 8021–8032.
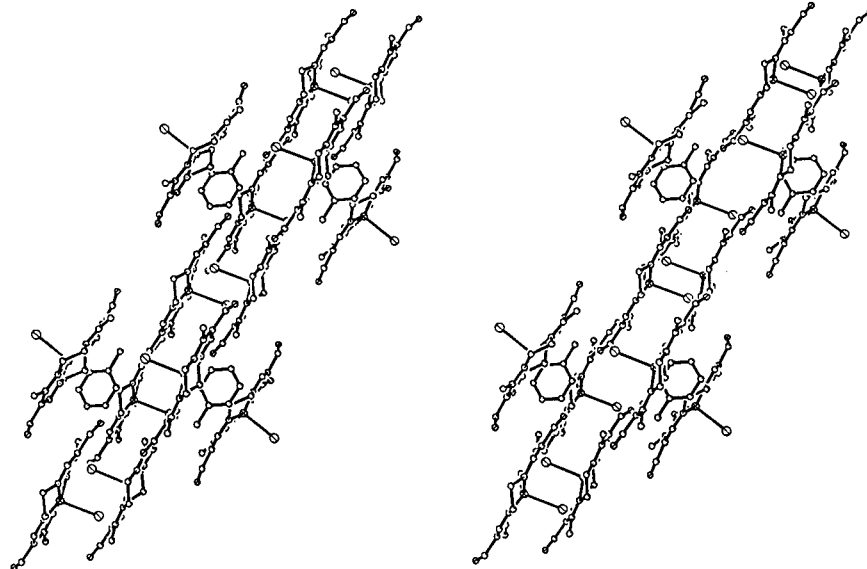
Figure 2. Stereoview of the molecule packing in the crystal of **3** (ethoxy groups omitted).

Table 3. Coordination Group Parameters of Various Pentacoordinated Iron(III) Complexes

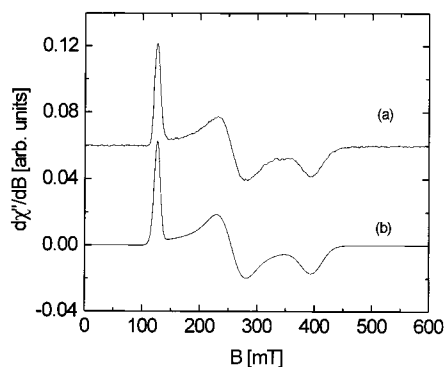| complex	spin state	Fe–N$_{eq}$, Å	Fe–L$_{ax}$, Å	Fe–ct, Å^a	ref
3 (L$_{ax}$ = I)	$\frac{3}{2}$	1.888/1.925	2.673	0.34	b
3(HIm)$_2$PF$_6$	$\frac{1}{2}$	1.883/1.913	2.004	0.00	33
2 (L$_{ax}$ = Cl)	$\frac{3}{2}$	1.926	2.406	0.38	16
1c (L$_{ax}$ = Cl)	$\frac{5}{2}$	2.002	2.252	0.60	34
I–FeTPP	$\frac{5}{2}$	2.066	2.554	0.46	5c
Cl–FeTPP	$\frac{5}{2}$	2.060	2.193	0.39	5b
Cl–FeOETPP	$\frac{5}{2}, \frac{3}{2}$	2.031	2.242	0.47	7
SbF$_6$–FeTPP	$\frac{5}{2}, \frac{3}{2}$	1.978	2.105	0.14	6b

^{a} ct = N$_4$-core plane. ^{b} This work.

Figure 3. EPR spectrum of **3** dissolved in toluene measured at T = 10 K (a) and simulated assuming Lorentzian line shape with g_y^{eff} = 5.38, g_x^{eff} = 2.70, and g_z^{eff} = 1.74 and line widths Γ_y = 10.7 mT, Γ_x = 47.5 mT, and Γ_z = 43.2 mT (b). Experimental conditions: microwave frequency 9.645 GHz; modulation frequency 100 kHz; modulation amplitude 10 G; microwave power 20 μW.

larger Fe–N$_{eq}$ distances are found than in the pure intermediate-spin complex **3**.

EPR Spectroscopy. The EPR spectrum of **3** in toluene is shown in Figure 3a. The simulation given in Figure 3b yields the effective g values g_y^{eff} = 5.38, g_x^{eff} = 2.70, and g_z^{eff} = 1.74. These values are characteristic for an $S = \frac{3}{2}$ ground state and can be analyzed with the spin Hamiltonian according to eq 1.

For $D \sim 10$ cm^{-1}, E/D = 0.22, and a slightly anisotropic $\tilde{g}$ = (2.03, 2.11, 2.00) eq 1 predicts effective g values g_y^{eff} = 5.38, g_x^{eff} = 2.68, and g_z^{eff} = 1.74 for the ground-state Kramers doublet of the $S = \frac{3}{2}$ system, in good agreement with the
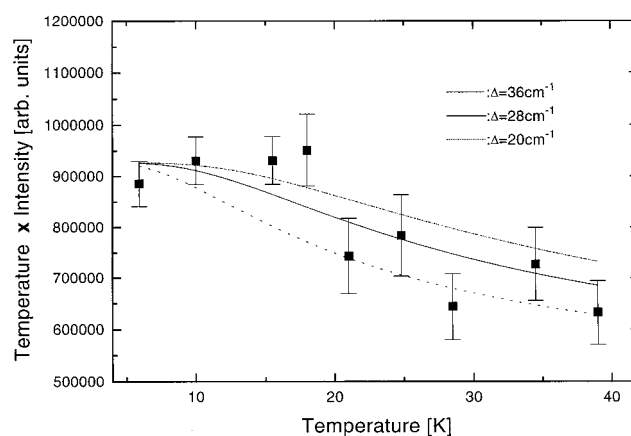

Figure 4. Temperature dependence of the product of temperature and observed intensity (IT) together with fits according to eq 4 (solid line). The obtained energy gap Δ = 28 cm^{-1} (solid line) leads to D = 13.4 cm^{-1} according to eq 5 with E/D = 0.22 cm^{-1}. The dash–dotted curve has been calculated with Δ = 20 cm^{-1} (D = 9.6 cm^{-1}), and the dashed curve, with Δ = 36 cm^{-1} (D = 17.2 cm^{-1}).

experimental data. Population of the second Kramers doublet would lead to resonances at g_y^{eff} = 1.38, g_x^{eff} = 1.16, and g_z^{eff} = 5.74 that could not be detected up to 10 K. The positive sign of D is confirmed by the variable-temperature study shown in Figure 4. The decrease of IT is caused by the depopulation of the ground-state Kramers doublet, as described by

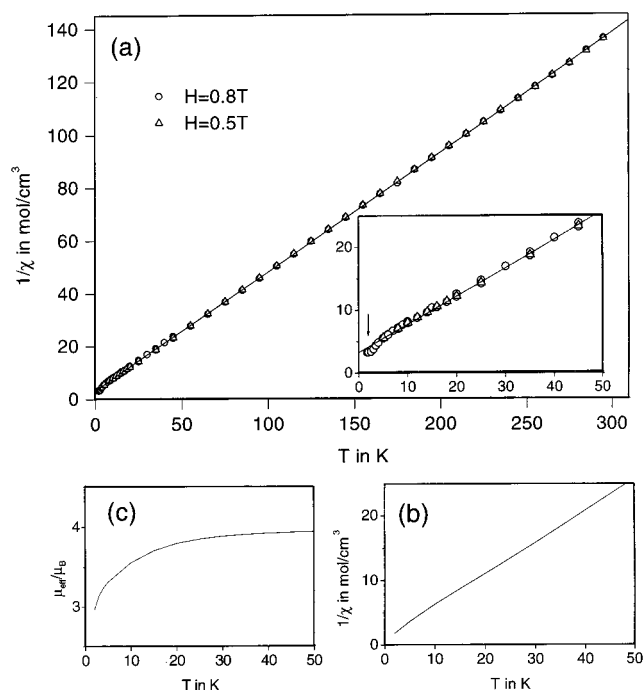$$IT \sim \frac{1}{1 + \exp\left(-\dfrac{\Delta}{k_B T}\right)} \quad (4)$$

The energy gap Δ between the two Kramers doublets is given as[35]

$$\Delta = 2\sqrt{D^2 + 2E^2} \quad (5)$$

Due to the scattering of the experimental data (Figure 4) only a rough estimate of D is possible (D = 13 ± 4 cm^{-1}).

(35) *Transition Ion Electron Paramagnetic Resonance*; Pilbrow, J. R.; Clarendon Press: Oxford, U.K., 1990; p 632.

Figure 5. (a) Inverse molar susceptibility versus temperature for **3** in the solid state and the Curie−Weiss fit. (b) Inverse molar susceptibility and (c) effective magnetic moment versus temperature calculated by diagonalization of eq 1 including powder averaging for $S = {}^3/_2$ spin system with $D = 13$ cm^{-1} and $E/D = 0.22$.

In the solid state **3** is EPR silent independently of the temperature down to 6 K. This solid-state effect may arise from magnetic ordering of the iron spins within and/or between the double layers in the crystalline state.

Magnetic Susceptibility Studies. In a previous paper[18] we reported **3** to be an intermediate-spin system ($S = {}^3/_2$) with ground state $^4A_2$ without any temperature dependence down to 77 K. These studies have now been extended to the temperature dependence of the susceptibility down to 1.73 K at 0.5 and 0.8 T. The graph of $1/\chi_M$ vs T for both fields is displayed in Figure 5. The plot is linear and independent of the field above ≈10 K and shows the expected linear dependence on T. From the Curie−Weiss law $1/\chi_M = T/C - \Theta/C$, the constants C and Θ were derived as $C = 2.224$ K cm^{-3} mol^{-1} and $\Theta = -7.37$ K. The effective magnetic moment remains constant down to 20 K ($\mu_{\text{eff}} = 4.19$ μ_B; "spin only" value, 3.87 μ_B) and confirms the ground state of $S = {}^3/_2$ for **3**. This behavior is represented by a spin-Hamiltonian simulation of $1/\chi(T)$ and $\mu_{\text{eff}}(T)$ for a $S = {}^3/_2$ spin system using $D = 13$ cm^{-1} and $E/D = 0.22$ as derived from the EPR study. At very low-temperature we found a behavior deviating from the Curie−Weiss law (see arrow in the inset of Figure 5a) with $1/\chi$ slightly decreasing (equivalent to an increase in χ) which is suggestive of ferromagnetic exchange. There appears to be a minimum in $1/\chi$ (i.e. a maximum in χ) with an incipient increase of $1/\chi$ at the lowest temperature that can be measured indicating the possible onset of antiferromagnetic ordering. This behavior correlates with the results of the EPR investigations. Whereas compound **3** in solution exhibits sharp signals at 10 K, the crystalline sample is EPR silent. Thus, the differing magnetic behavior may be explained with magnetic ordering due to intermolecular interactions in the crystal packing. The crystal structure shows the arrangement of the molecules in double layers with opposite orientation of the Fe−I bonds in the neighboring layers and a very short interlayer distance of 2.92 Å (Figure 2). On this basis,
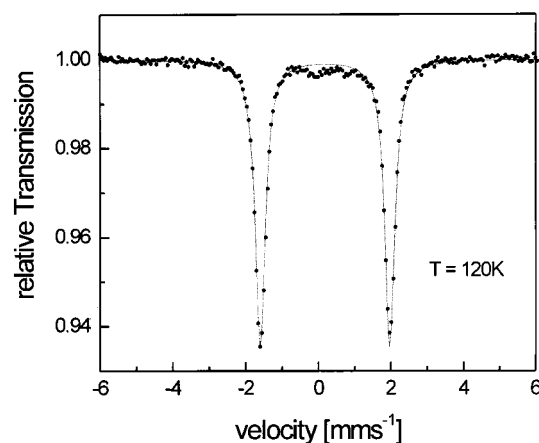
Figure 6. Mössbauer spectrum of **3** in the solid state measured at 120 K in a field of 20 mT $\perp \gamma$. The solid line is a Lorentz fit with $\delta = 0.18(4)$ mms^{-1}, $\Delta E_Q = 3.56(7)$ mms^{-1}, and $\Gamma = 0.33(4)$ mms^{-1}.

the reason for the magnetic ordering can be related to interactions between oppositely oriented molecules inside the double layers. A similar magnetic behavior at low temperature was found in the case of the related complexes **1** without the carbonyl groups[15] and the halides of iron(III) thiocarbamates.[12d]

Mössbauer Spectroscopy. The Mössbauer spectrum of **3** obtained at 120 K (Figure 6) exhibits a doublet with an isomer shift $\delta = 0.18$ mm/s and a quadrupole splitting $\Delta E_Q = 3.56$ mm/s.

The high value of ΔE_Q compares well with that reported for **2** ($\delta = 0.14$ mm/s and $\Delta E_Q = 3.68$ mm/s at 298 K), which exhibits an intermediate-spin ($S = {}^3/_2$) ground state.[16] This is confirmed by the spin-Hamiltonian analysis of the spectra taken from 4.2 K up to 180 K in a field of 7 T parallel to the γ-ray (Figure 7). The temperature dependence is well reproduced by spin-Hamiltonian simulations assuming a $S = {}^3/_2$ spin system with a zero field splitting of $D = 13$ cm^{-1} and the rhombicity parameter $E/D = 0.22$ taken from the EPR analysis. The analysis of the spectra leads to a positive sign of ΔE_Q, $\eta = 0$, and an axial hyperfine-coupling tensor $\tilde{A}/\mu_N g_N = (-12.7, -12.7, 0.5)$ T. Allowing the A tensor to be anisotropic did not improve the quality of the simulations. The small deviations of the simulated and the experimental data may be possibly due to spin−spin relaxation effects in the solid state.

Molecular Orbital Calculations. The complex **3** contains 54 atoms and 143 valence orbitals and requires 87 s CPU time per iteration on a VAX6000/610 machine. Unless otherwise noted, the calculations are based on the experimental geometry. The z-axis of the molecular coordinate system is chosen in direction of the Fe−I bond, and the (x,y)-plane is defined by the average plane through the four nitrogen atoms of the macrocycle. The iron atom is then located 0.34 Å above the (x,y)-plane. The x- and y-axes are directed between the nitrogens with the y-axis pointing toward C4 (cf. Figure 1) so that the σ-bonds with the macrocycle are formed by the $3d_{xy}$ orbital of iron. The central purpose of the subsequent investigations is to understand the reasons for the intermediate spin state and to describe its properties on the basis of a spin-unrestricted MO treatment in more detail since the electronic structure of intermediate spin state systems is still not fully understood.

A first attempt to rationalize the intermediate spin state consists of analyzing the MO energies. A spin-restricted calculation (left part of Figure 8) yields the typical pattern of a slightly distorted square pyramidal coordination with a weak
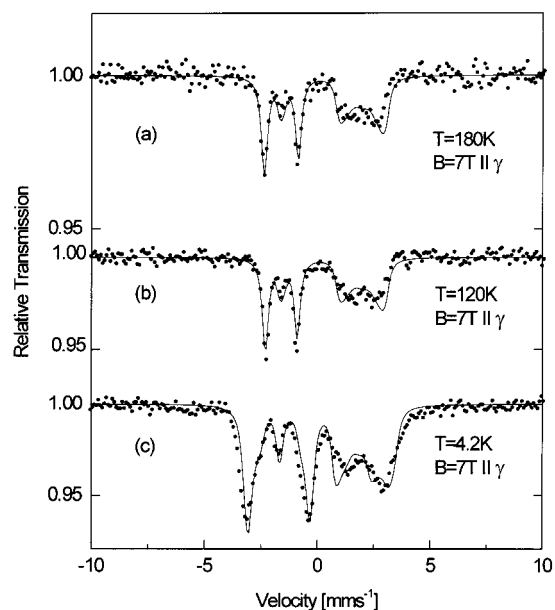
Figure 7. Mössbauer spectra of **3** in the solid state recorded at 4.2, 120, and 180 K in a field of 7 T parallel to the γ-beam. The solid lines are spin-Hamiltonian simulations for a $S = {}^3/_2$ spin system with $D = 13$ cm^{-1}, $E/D = 0.22$, $\tilde{g} = (2.03, 2.11, 2.00)$, $\tilde{A}/\mu_{\text{NgN}} = (-12.7, -12.7, 0.5)$ T, $\delta = 0.19$ mms^{-1}, $\Delta E_Q = +3.56$ mms^{-1}, $\eta = 0$, and $\Gamma = 0.32$ mms^{-1}.
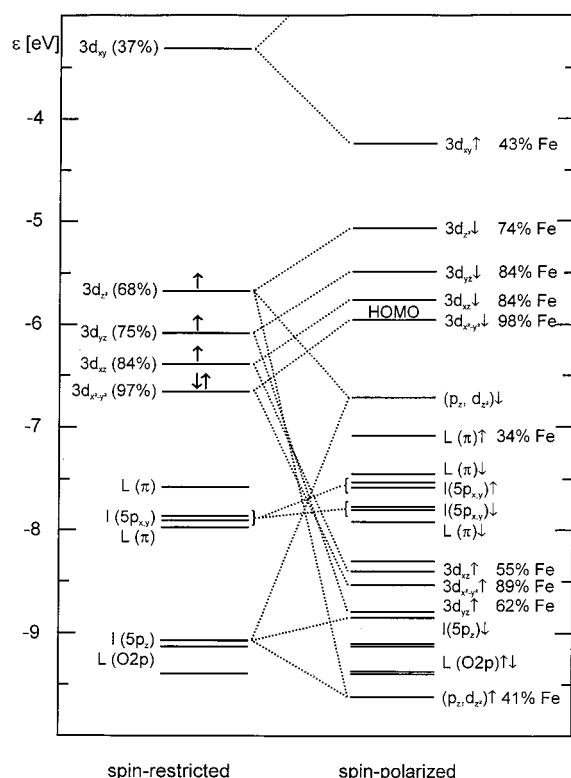
Figure 8. Orbital energies between -3 and -10 eV for the $S = {}^3/_2$ ground state of **3**. The approximate assignment for each level is given (L denotes the equatorial ligand of **3**) together with the Fe(3d) percentage for those orbitals with predominant d character.

axial ligand. The σ-antibonding $3d_{xy}$ orbital of iron is well separated from the other four d orbitals. Among these the lowest in energy is the (doubly occupied) nonbonding $3d_{x^2-y^2}$ orbital followed by the two weakly π-antibonding $3d_{xz,yz}$ orbitals and

Table 4. Orbital Energies ϵ_i and Composition (in %) of the Relevant Spin-Up (Left) and Spin-Down (Right) Orbitals with the HOMO's marked by an Asterisk

ϵ_i [eV]	Fe(3d)	I(5p)	N(2p)	ϵ_i [eV]	Fe(3d)	I(5p)	N(2p)
-4.25	43(xy)		38	-2.36	47(xy)		32
-6.72^*	34(z^2)	27	18	-5.07	74(z^2)	16	4
-7.08	25(yz)	1	35	-5.49	84(yz)	3	6
-7.53	20(xz)	76	2	-5.76	84(xz)	6	2
-7.58	6(yz)	87	4	-5.96^*	98($x^2 - y^2$)		
-8.31	37(mix)	13	18	-7.45	8		43
-8.40	55(xz)	14	11	-7.77	3	94	
-8.54	89($x^2 - y^2$)	1	2	-7.81	2	94	1
-8.79	62(yz)	10	7	-7.92	8	9	35
-9.12	1		1	-8.85	7	75	5
-9.39	1		1	-9.10			1
-9.62	41(z^2)	52	1	-9.38			1

by the $3d_{z^2}$ orbital involved in the σ-bond with the axial ligand. These three orbitals are singly occupied in a spin-restricted calculation. The $3d_{yz}$ orbital makes a slightly stronger interaction with the macrocycle than the $3d_{xz}$ orbital as indicated by the larger destabilization by 0.45 eV and a reduced iron contribution. The equatorial ligand has two high-lying MOs similar to porphyrin, and the 5p orbitals of the axial ligand are split into the strong σ-bonding $5p_z$ and into the nearly nonbonding $5p_{x,y}$ orbitals.

A more detailed picture is provided by the spin-polarized calculation (right part of Figure 8). The gross pattern of the spectrum is now dominated by the exchange splitting of the 3d orbitals of iron which is largest between the nonbonding $3d_{x^2-y^2}$ orbitals with 2.58 eV. The stabilization of the majority spin ("spin-up") orbitals leads to strong covalent interactions of the $3d_{xz,yz}$ and $3d_{z^2}$ orbitals with the ligand orbitals as indicated by the reduced iron participation in these orbitals compared with the spin-restricted calculation, as well as by the participation of the 3d↑ orbitals in several other ligand orbitals (Table 4). Especially, the $3d_{z^2}$ orbital undergoes a rather strong interaction with the I($5p_z$) orbital resulting in a splitting of 2.9 eV between the bonding and antibonding MOs, and the $3d_{yz}$↑ orbital is the lowest within the t_{2g}-type manifold.

At the same time the destabilization of the minority spin ("spin-down") orbitals is accompanied by a slight increase of their Fe(3d) character. The splitting between the highest occupied MO (HOMO) $3d_{x^2-y^2}$↓ and the $3d_{xy}$↑ orbitals is 1.71 eV. This energy difference required for the transition to the high-spin state is not compensated by the increased exchange splitting in the high-spin state. Additionally, the strongly antibonding nature of the $3d_{xy}$↑ orbital is energetically unfavorable for realizing the high-spin state, as commonly met in the five-coordinated Fe porphyrins. Another remarkable difference compared with the porphyrins is the orientation of the $3d_{xz,yz}$ orbitals that are directed between the coordinating nitrogens of the macrocycle instead of toward them.

Altogether this analysis shows that two factors are responsible for the intermediate-spin state of **3**. The first condition is a strong equatorial ligand as provided by the reduced π-system[18] and the smaller 14-membered macrocycle of **3**.[36] This is reflected in the short Fe—N bond distances in **3** and leads to the large destabilization of the σ-antibonding $3d_{xy}$ orbital[37] of iron preventing that the high-spin state becomes the ground state as in most five-coordinated Fe(III) porphyrins. The second condi-

(36) In presence of analogous axial ligands, the 16-membered macrocycles **1** stabilize more effectively the high-spin state.[14]

(37) (a) Minin, W. W.; Rakitin, J. W.; Wolkow, W. W.; Larin, G. M. *Isv. Akad. Nauk* **1980**, *10*, 2205−2212. (b) Minin, W. W.; Rakitin, J. W.; Larin, G. M.; Jäger, E.-G. *J. Neorg. Chim.* **1981**, *26*, 650−658.

Table 5. Binding Energies (in eV),[a] Effective Charges Q, Overlap Populations P, d-Shell Occupation n, and d-Shell Spin Density m of Iron for the Three Spin States of **3**

spin	$\Delta E_B(z_{exp})$	$\Delta E_B(z_{calc})$	z_{calc}, Å	Q(Fe)	Q(I)	Q(N)	P(FeI)	P(FeN)	n(Fe3d)	m(Fe3d)
$3/2$	0.00	−0.02	0.31	0.406	−0.653	−0.171	0.200	0.414	6.24	2.71
$5/2$	1.60	1.51	0.43	0.608	−0.621	−0.204	0.176	0.339	6.02	3.82
$1/2$	2.09	1.91	0.22	0.331	−0.570	−0.171	0.232	0.431	6.26	1.07

[a] Relative to the intermediate spin state at the experimental geometry; the experimental value z_{exp} of the z-coordinate of iron relative to the plane of the macrocycle is 0.34 Å.

tion is a sufficiently weak axial ligand so that the $3d_{z^2}$ orbital remains close enough to the other three 3d orbitals, whereas a strong axial ligand would destabilize this orbital so much that a low-spin state would result. Similar conclusions have previously been derived within a ligand-field treatment.[10,37]

In the next step it is necessary to confirm theoretically the $S = 3/2$ ground state by comparing the total energies of the different spin states. The results displayed in Table 5 show that in fact both the high-spin ($S = 5/2$) and the low-spin ($S = 1/2$) state are lying distinctly above the ground state by 1.60 eV ($S = 5/2$) and 2.09 eV ($S = 1/2$), respectively. However, the actual energy differences may be smaller since especially the position of iron with respect to the plane of the macrocycle is expected to depend on the spin state. Therefore, the iron position has been optimized keeping all the other distances fixed. The calculated z-coordinate z_{calc} for the $S = 3/2$ ground state is close to the experimental value. In the low-spin state the iron moves toward the macrocycle by about 0.1 Å, while for the high-spin state the iron is removed by about the same amount. The last result is easy to understand since the (destabilizing) antibonding σ-interaction of the Fe($3d_{xy}$) orbital is reduced upon increasing the distance of iron to the macrocycle. The energy spacing between the various spin states is then slightly reduced, but the ordering remains the same.

Further insight can be obtained by comparing the charge and spin density distribution in the three spin states (Table 5). First of all, the bonding of iron becomes more ionic with increasing spin state as can be concluded from the increased charge of iron, the reduced overlap populations, and the reduced 3d-shell population. The transition from the intermediate-spin to the low-spin state mainly concerns the Fe−I bond since an electron is removed from the σ-antibonding ($5p_z,3d_{z^2}$) orbital. This is in accordance with the above-mentioned observation that the Fe−N_{eq} distances in the intermediate-spin **3** and in the low-spin **3**(Him)$_2$PF$_6$ are virtually identical (Table 3). In the high-spin state the σ-antibonding ($2p_{x,y},3d_{xy}$) orbital is populated so that the Fe−N bonds are weakened. The spin density at the low-spin iron shows a small "overspill" that is compensated by negative spin densities at the iodine and the nitrogens, while in the higher spin states the spin densities are considerably reduced compared with the formal values of 3 and 5, respectively, mainly due to covalent interactions of the $3d\downarrow$ orbitals with the ligand MO's. Together with the relatively small effective charges of iron this shows that the bonding in **3** exhibits rather strong covalent character.

Similar conclusions are reached when analyzing the electric field gradients. The calculated quadrupole splitting ΔE_Q of +2.64 mm/s is in qualitative agreement with the experimental value. The direction of the main component V_{zz} of the electric field gradient (efg) tensor deviates by 11° from the Fe−I axis due to the nonplanarity of the macrocycle. In the principal axes system of the efg tensor the efg can be decomposed with respect to a basis of atomic orbitals into three parts, denoted as valence, covalency, and ligand contributions,[30] and ΔE_Q correlates directly with the sum of these three contributions. The valence

Table 6. Calculated Quadrupole Splitting (in mm/s), Asymmetry Parameter η, d-Shell Anisotropy Δn_d, and efg Contributions for the Three Spin States of **3**

spin	ΔE_Q	η	Δn_d	valence	covalency	ligand
$3/2$	+2.64	0.40	0.59	2.14	0.50	0.00
$5/2$	+0.87	0.53	−0.07	0.25	0.52	0.10
$1/2$	(+)4.13[a]	0.96	0.73	3.48	0.58	0.06

[a] Sign not given because $\eta \approx 1$.

part is roughly proportional to the anisotropy $\Delta n_d = n_{x^2-y^2} + n_{xy} - n_{z^2} - (n_{xz} + n_{yz})/2$ of the Fe(3d) shell occupation. Within the frame of the ligand-field model the formal 3d-orbital occupation numbers for Fe(III) in the $S = 3/2$ state are $n_{x^2-y^2}^2$ $n_{z^2\uparrow}^1$ $n_{xz\uparrow}^1$ $n_{yz\uparrow}^1$ so that a vanishing Δn_d would result. This has occasionally led to the conclusion that five-coordination can result in a large ligand-field contribution to the efg.[38] On the basis of the MO calculations one arrives at a completely different picture.

First, the occupation of the formally occupied orbitals is $n_{x^2-y^2}^{1.97}$ $n_{z^2\uparrow}^{0.98}$ $n_{xz\uparrow}^{0.97}$ $n_{yz\uparrow}^{0.97}$ resulting in a small Δn_d of 0.015. On the other hand, the actual occupation of the formally empty levels is obtained as $n_{xy}^{0.90}$ $n_{z^2\downarrow}^{0.21}$ $n_{xz\downarrow}^{0.09}$ $n_{yz\downarrow}^{0.1}$ yielding $\Delta n_d = 0.575$ which corresponds roughly to a quadrupole splitting of 2.3 mm/s and originates from the covalent mixing of the formally empty 3d orbitals (mainly of the σ-interacting $3d_{xy}$ orbital) interacting with the doubly occupied ligand MO's.

The analysis of the exact results (Table 6) confirms this qualitative estimate, viz. a dominating valence contribution of 2.14 mm/s and a relatively large covalency contribution of 0.50 mm/s while the ligand contribution is merely 0.002 mm/s. It should also be mentioned that almost 25% of the valence contribution arises from the anisotropy of the Fe(4p)-shell occupation.

Altogether, these results confirm the strong covalent character of the bonding between iron and the macrocycle so that a ligand-field model turns out to be inappropriate for the interpretation of the efg of this complex, even though it might be useful in other respect.

The quadrupole splittings of the other spin states follow the usual expectations, i.e., ΔE_Q is small for the high-spin and large for the low-spin state. Again the ligand contributions are small in both cases. For the high-spin state the d-shell anisotropy Δn_d is negative albeit rather small and the positive valence contribution is solely due to the anisotropy of the 4p shell with $\Delta n_p = 0.17$. As a consequence the efg is dominated by the covalency contribution emphasizing the importance of covalency even in the more ionic high-spin species.

Conclusions

Complex **3** was structurally characterized as a pentacoordinated iron(III) complex. Its pure intermediate-spin state ($S = 3/2$) was proven by temperature-dependent magnetic susceptibil-

(38) Riley, D. P.; Merrell, P. H.; Stone, J. A.; Busch, D. H. *Inorg. Chem.* **1975**, *14*, 490.

ity and EPR measurements as well as by Mössbauer spectroscopy. The MO calculations supply a detailed insight into the bonding modes and intramolecular interactions. The electronic structure around the iron center is well described, as indicated by the correct determination of the ground state and by the qualitative agreement between the measured and calculated quadrupole splitting. Evaluation of magnetic behavior and EPR spectra at low temperature indicates a magnetic ordering in the solid state that can be explained by intermolecular interactions inside of the double layers of complex molecules in the crystal.

Supporting Information Available: Tables SI−SV, listing crystal and structure refinement data, atomic coordinates ($\times 10^4$) and equivalent isotropic displacement parameters ($\text{Å}^2 \times 10^3$), bond lengths (Å) and angles (deg), anisotropic displacement parameters ($\text{Å}^2 \times 10^3$), and hydrogen coordinates ($\times 10^4$) and isotropic displacement parameters ($\text{Å}^2 \times 10^3$) for **3**, and X-ray crystallographic files in CIF format. This material is available free of charge via the Internet at http://pubs.acs.org.

IC981276Z